ARTICLES
https://doi.org/10.1038/s41563-021-00934-3

nature materials

Check for updates

Thermally conductive ultra-low-*k* dielectric layers based on two-dimensional covalent organic frameworks

Austin M. Evans[1,19], Ashutosh Giri[2,3,19], Vinod K. Sangwan[4], Sangni Xun[5,6,7], Matthew Bartnof[8], Carlos G. Torres-Castanedo[4], Halleh B. Balch[9,10,11], Matthew S. Rahn[4], Nathan P. Bradshaw[4], Edon Vitaku[1], David W. Burke[1], Hong Li[12], Michael J. Bedzyk[4,13], Feng Wang[9,10,11], Jean-Luc Brédas[12], Jonathan A. Malen[8,14], Alan J. H. McGaughey[8,14], Mark C. Hersam[1,4,15,16], William R. Dichtel[1]✉ and Patrick E. Hopkins[2,17,18]✉

As the features of microprocessors are miniaturized, low-dielectric-constant (low-*k*) materials are necessary to limit electronic crosstalk, charge build-up, and signal propagation delay. However, all known low-*k* dielectrics exhibit low thermal conductivities, which complicate heat dissipation in high-power-density chips. Two-dimensional (2D) covalent organic frameworks (COFs) combine immense permanent porosities, which lead to low dielectric permittivities, and periodic layered structures, which grant relatively high thermal conductivities. However, conventional synthetic routes produce 2D COFs that are unsuitable for the evaluation of these properties and integration into devices. Here, we report the fabrication of high-quality COF thin films, which enable thermoreflectance and impedance spectroscopy measurements. These measurements reveal that 2D COFs have high thermal conductivities (1 W m^{-1} K^{-1}) with ultra-low dielectric permittivities ($k = 1.6$). These results show that oriented, layered 2D polymers are promising next-generation dielectric layers and that these molecularly precise materials offer tunable combinations of useful properties.

To take advantage of sub-10 nanometre integrated circuit components, interlayer low-dielectric-constant (low-*k*) materials with high thermal conductivities must be developed[1–3]. As dielectric layers have become thinner, electronic crosstalk and capacitive signal delay substantially diminish device performance. The Semiconductor Industry Association has identified the development of mechanically robust, thermally stable, few-nanometre, low-*k* ($k < 2.4$) and ultra-low-*k* ($k < 1.9$) materials as needed to address this challenge[4,5]. Ultimately, the realization of such materials will reduce parasitic capacitance, which enables faster gate operations and minimizes dynamic power dissipation[1,6,7]. Therefore, the advancement of low-*k* dielectric materials and thin-film (<200 nm) fabrication techniques is necessary[1–3]. Towards this end, two major classes of low-*k* dielectric materials have been developed: organic materials that are inherently low-*k* owing to limited polarizability, and porous oxides that are low-*k* as a result of their large free volumes. However, all known low-*k* materials have large thermal resistances that arise from their disordered morphologies and high porosities[8–11], which limit high-power-density chip performance owing to inadequate heat management[2–5].

Two-dimensional (2D) covalent organic frameworks (COFs) are a class of modular, molecularly precise, highly porous, layered polymer sheets[12,13]. These attributes impart a combination of physical properties unseen in conventional polymers, such as high thermomechanical stabilities and low densities[12]. Challenges associated with characterizing conventionally isolated polycrystalline COF powders have restricted the exploration of many 2D COF properties. To address this challenge, COFs have been fabricated as thin films via direct growth[14,15], exfoliation[14,16,17], or interfacial polymerization[15,18,19]. However, none of these methods have proven to be general for wafer-scale synthesis of oriented and crystalline COF films without powder contamination. Synthetic limitations have hindered the evaluation of the fundamental properties of COFs related to their use as low-*k* dielectric layers[20], even as Wang and coworkers demonstrated preliminary promise in the use of 2D COFs for this purpose[21].

[1]Department of Chemistry, Northwestern University, Evanston, IL, USA. [2]Department of Mechanical and Aerospace Engineering, University of Virginia, Charlottesville, VA, USA. [3]Department of Mechanical, Industrial and Systems Engineering, University of Rhode Island, Kingston, RI, USA. [4]Department of Materials Science and Engineering, Northwestern University, Evanston, IL, USA. [5]School of Chemistry and Biochemistry, Georgia Institute of Technology, Atlanta, GA, USA. [6]Center for Organic Photonics and Electronics, Georgia Institute of Technology, Atlanta, GA, USA. [7]College of Environmental Science and Engineering, Hunan University, Changsha, People's Republic of China. [8]Department of Mechanical Engineering, Carnegie Mellon University, Pittsburgh, PA, USA. [9]Department of Physics, University of California Berkeley, Berkeley, CA, USA. [10]Kavli Energy NanoScience Institute, University of California Berkeley, Berkeley, CA, USA. [11]Materials Sciences Division, Lawrence Berkeley National Laboratory, Berkeley, CA, USA. [12]Department of Chemistry and Biochemistry, The University of Arizona, Tucson, AZ, USA. [13]Department of Physics and Astronomy, Northwestern University, Evanston, IL, USA. [14]Department of Materials Science and Engineering, Carnegie Mellon University, Pittsburgh, PA, USA. [15]Department of Electrical and Computer Engineering, Northwestern University, Evanston, IL, USA. [16]Simpson Querrey Institute, Northwestern University, Evanston, IL, USA. [17]Department of Physics, University of Virginia, Charlottesville, VA, USA. [18]Department of Materials Science and Engineering, University of Virginia, Charlottesville, VA, USA. [19]These authors contributed equally: Austin M. Evans, Ashutosh Giri. ✉e-mail: wdichtel@northwestern.edu; peh4v@virginia.edu

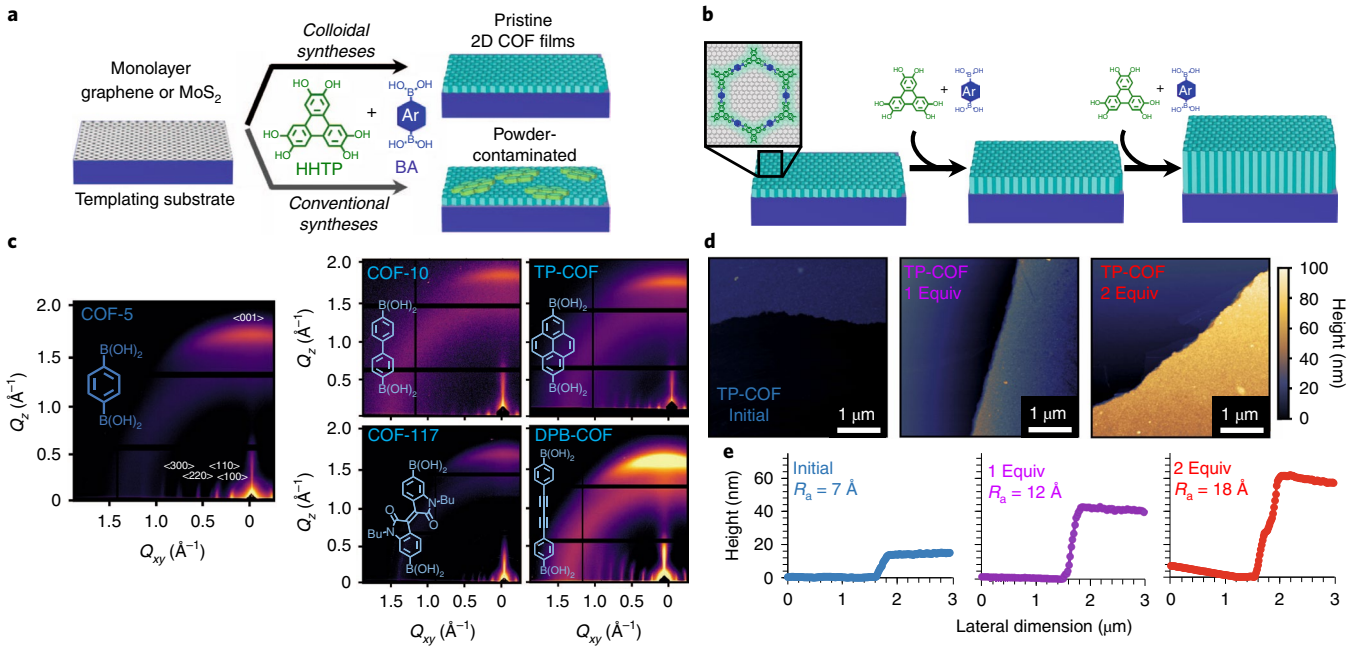

Fig. 1 | Templated colloidal polymerization of boronate ester-linked COF films. a,**b**, Synthesis of boronate ester-linked COF films (**a**) and the sequential polymerization of 2D COF films by repeated introduction of monomer (**b**). **c**, GI-WAXS patterns of COF films. **d**, Atomic force micrographs of sequentially polymerized TP-COF films. **e**, Line cuts of sequentially polymerized TP-COF films in **d**. AR, aryl; BA, boronic acid; Equiv, equivalent polymerization.

Here, we synthesize high-quality wafer-scale boronate ester-linked 2D COF films through a templated colloidal approach. Previously, we had found that supported graphene substrates template the formation of oriented 2D COF thin films[15]. However, films obtained by this method are often unsuitable for device measurements because of contamination by insoluble COF powders that form during the synthesis. Recently, we found that nitrile cosolvents prevent the precipitation of insoluble products and instead provide COFs as solution-stable colloidal suspensions[20,22–24]. Here, we use colloidal approaches to grow COF thin films with roughnesses of a few nanometres and with controllable thicknesses on device-relevant substrates without precipitate contamination. This approach is demonstrated for five 2D COFs, including a previously unreported structure, which are synthesized on both graphene and monolayer MoS_2. Furthermore, these 2D COF films are amenable to sequential polymerization cycles, which enables nanometre-precise thickness control not possible in traditional precipitant-contaminated solvothermal syntheses.

The unprecedented quality of these films enables the measurement of thermomechanical and optoelectronic properties of COF films. Optical absorption and emission spectroscopies show that boronate ester-linked COF films are electronically insulating. These results are consistent with density functional theory (DFT) calculations that predict that pristine COF-5 films, which are produced by the condensation of 2,3,6,7,10,11-hexahydroxytriphenylene (HHTP) and 1,4-phenylenebisboronic acid (PBBA), have an indirect electronic bandgap of 3.6 eV and a direct bandgap of 3.9 eV. Impedance spectroscopy performed on COF-5 thin films reveals that they are electronically insulating, ultra-low-k ($k < 1.7$) dielectric layers; these results are consistent with DFT-calculated low electronic dielectric tensors ($\varepsilon_{xx,yy,zz} < 2$) for all COFs investigated.

Owing to their regularly porous, covalently linked, layered structure, 2D COFs circumvent the low thermal conductivities that afflict leading low-k dielectrics. By using time-domain and frequency-domain thermoreflectance (TDTR and FDTR, respectively) and molecular dynamics simulations, we find that 2D COFs have a combination of low densities ($\rho < 1\,g\,cm^{-3}$) and relatively high thermal conductivities ($\kappa > 0.8\,W\,m^{-1}\,K^{-1}$ in the cross-plane direction with a predicted anisotropy ratio of >3 in the in-plane direction). These findings show that 2D COFs are promising as ultra-low-k dielectrics with desirable heat management characteristics. More broadly, access to high-quality 2D COF thin films provides a means to rationally design solid-state organic materials to unlock technologically useful combinations of properties.

Colloidal polymerization methods

All 2D COF films were polymerized directly by a templated colloidal approach. First, a SiO_2-supported graphene or an Al_2O_3-supported monolayer MoS_2 was submerged into a solution of HHTP and a difunctional arylboronic acid (Fig. 1a and Supplementary Figs. 9–14). The polymerization mixtures were then sealed and heated to 85 °C for 12 h. Finally, the substrate was removed from the reaction mixture, rinsed with clean solvent and dried. Prior to robust structural characterization, we observed that an optically homogenous film had formed across the entire substrate (Supplementary Fig. 16). To probe whether these films were being polymerized from solution or whether colloidal species were templating on the surface, we immersed a graphene-supported substrate in a prepolymerized colloidal 2D COF suspension and subjected the substrate to the polymerization conditions; this did not produce COF films. These observations suggest that homogenous nucleation occurs in solution and templated-heterogeneous nucleation occurs on the substrate simultaneously, which then polymerize independently.

All 2D COF films are found to be crystalline, oriented, and smooth. Atomic force microscopy (AFM) reveals that the materials are obtained as thin films (<75 nm) with <5 nm root-mean-square roughness in all cases (Supplementary Figs. 20 and 22–25). The 2D grazing-incidence wide-angle X-ray scattering (GI-WAXS) patterns of all COFs showed prominent in-plane Bragg diffraction features concentrated along the Q_{xy} axis and cross-plane Bragg features concentrated along the Q_z axis (Fig. 1c and Supplementary Figs. 26–31), which reveals that 2D COF layers are oriented parallel

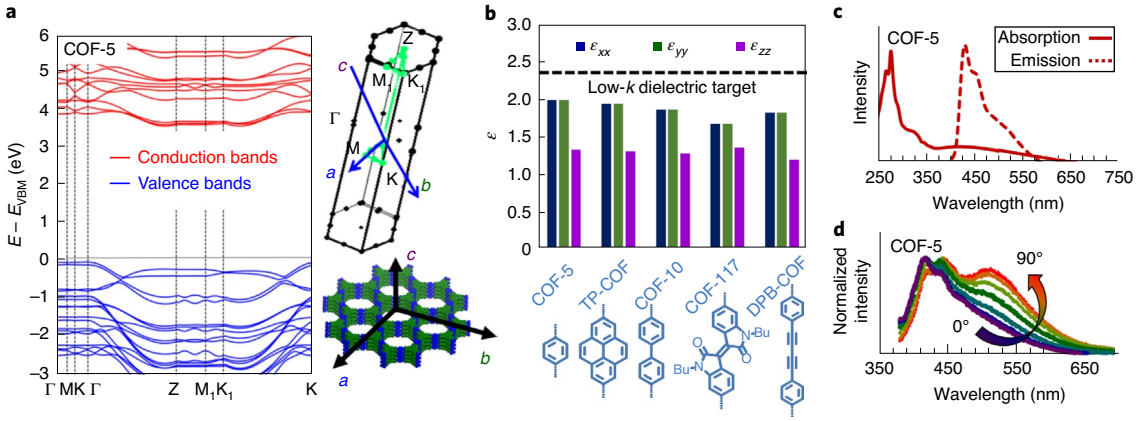

Fig. 2 | Optoelectronic properties of COF films. a, Electronic band structures calculated at the DFT/PBE0 level for COF-5 and the corresponding Brillouin zone. VBM, valence band maximum. **b**, Electronic dielectric tensors calculated at the DFT/PBE level for all COFs studied. **c**, Optical absorption and emission ($\lambda_{excitation}$ = 325 nm) profiles for COF-5. **d**, Polarization-dependent emission of COF-5 films that resolves the in-plane (purple, 0°) component from the cross-plane (red, 90°) component.

to the substrate. By assessing the azimuthal dispersity of the interlayer <001> Bragg feature (~2 Å^{-1}) intensity, we find that these films have a smaller full-width at half-maximum than those reported by other approaches. We attribute the weaker orientation of previously prepared films to the contamination by unoriented precipitates formed during their synthesis (Supplementary Fig. 35)[14,15]. In all cases, radially integrated diffraction patterns were found to agree well with simulated COF diffraction patterns, which confirmed the successful synthesis of the expected COF networks (Supplementary Figs. 37–41). The large number and sharp line shapes of diffraction features observed in these patterns indicate that COF films prepared by colloidal methods are highly crystalline. Collectively, these films are homogenous, crystalline and oriented.

The high quality of these films allows for sequential growth by the introduction of unreacted monomers (Fig. 1b). Typically, COF film thickness is controlled by modifying the starting monomer concentration used for their polymerization. However, when we attempted to polymerize COF-5 films with higher monomer concentrations, we found that resultant COF films, although thicker, were substantially less oriented and less smooth (Supplementary Fig. 34). This finding is consistent with our recent observations of uncontrolled nucleation and growth at higher monomer concentrations[22,25]. However, by polymerizing COF films using this templated growth approach, removing the substrate, immersing this substrate in a fresh monomer solution, and resubjecting it to the polymerization conditions, we can continue the polymerization of our films without a reduction in film quality. As an example, we sequentially increase the thickness of the TP-COF films, which are polymerized from 2,3,6,7,10,11-hexahydroxytriphenylene and pyrene-2,7-diboronic acid, from 20 nm to 40 nm and then to 60 nm over the course of three equivalent polymerizations (Fig. 1d,e). In each sequential polymerization, we find that the roughness, crystallinity and film orientation as evaluated by AFM and GI-WAXS do not change discernably (Supplementary Figs. 31–33). Collectively, these observations demonstrate that templated colloidal polymerization offers a level of synthetic control not available in previously reported 2D polymerization strategies.

Electronic properties

The boronate ester-linked 2D COF films studied here are sufficiently electrically insulating to serve as dielectric layers. DFT calculations using the PBE0 functional (which is based on the Perdew–Burke–Ernzerhof functional) predict that COF-5 has an indirect bandgap of 3.6 eV and a direct gap of 3.9 eV (Fig. 2a). The DFT-calculated band structures have minimal band dispersion along the in-plane direction (Γ-M-K-Γ and Z-M$_1$-K$_1$) in both their valence and conduction bands, which indicates low in-plane charge-carrier mobility. However, band dispersions of 0.4 eV along the out-of-plane direction in both the valence and conduction bands can be observed, which suggests that anisotropic charge transport may occur through the COF-5 layers, as has been observed previously[22]. The DFT-calculated diagonal components of the static electronic dielectric tensors (ε_{xx}, ε_{yy} and ε_{zz}) are less than 2 for the five boronate ester-linked 2D COFs that were studied. As such, they are all candidate low-k dielectrics (Fig. 2b). We note that in COF-5 the ionic contribution to the total static dielectric tensor is calculated to be negligible (Supplementary Table 3); therefore, we considered only the electronic contribution to the dielectric tensor in the other four 2D COFs. Experimentally, we find that the first COF-5 optical absorption feature occurs at approximately 325 nm (3.8 eV), which is consistent with the predicted DFT direct bandgap (Fig. 2c). When the COF-5 structure is excited at 325 nm, we find that its emission profile is similar to that of monomeric HHTP, which is consistent with the limited electronic conjugation across boronate ester bonds[26]. Ultimately, these experimental and computational studies show that crystalline, 2D COF layers are promising as low-k dielectrics.

The pristine nature of the films prepared by colloidal syntheses permits the observation of their anisotropic optical emission. The polarization-dependent emission of a COF-5 film has a strong cross-plane emission feature at 530 nm, which has been assigned previously to the formation of triphenylene exciplexes (Fig. 2d)[26]. The observation of these cross-plane features suggests that the COF-5 films are highly oriented across the entire sample. By contrast, polarization-dependent emission anisotropy is found to be much weaker in COF-5 films grown on the substrates under non-colloidal conditions (Supplementary Fig. 43)[15]. This finding agrees with our understanding that previously obtained materials were likely contaminated with unoriented aggregates, which complicated their reliable measurement and subsequent integration into devices.

Impedance measurements conducted on parallel plate capacitors confirm that COF-5 is a low-k dielectric. First, we synthesized COF-5 thin films directly onto epitaxially grown graphene (EG) on doped SiC wafers. Next, a 6-nm-thick Al_2O_3 layer was deposited by atomic layer deposition (to prevent shorting through the COF-5 pores) before top Au electrodes were deposited onto the Al_2O_3, which produced a series of devices over an area of 40 mm^2

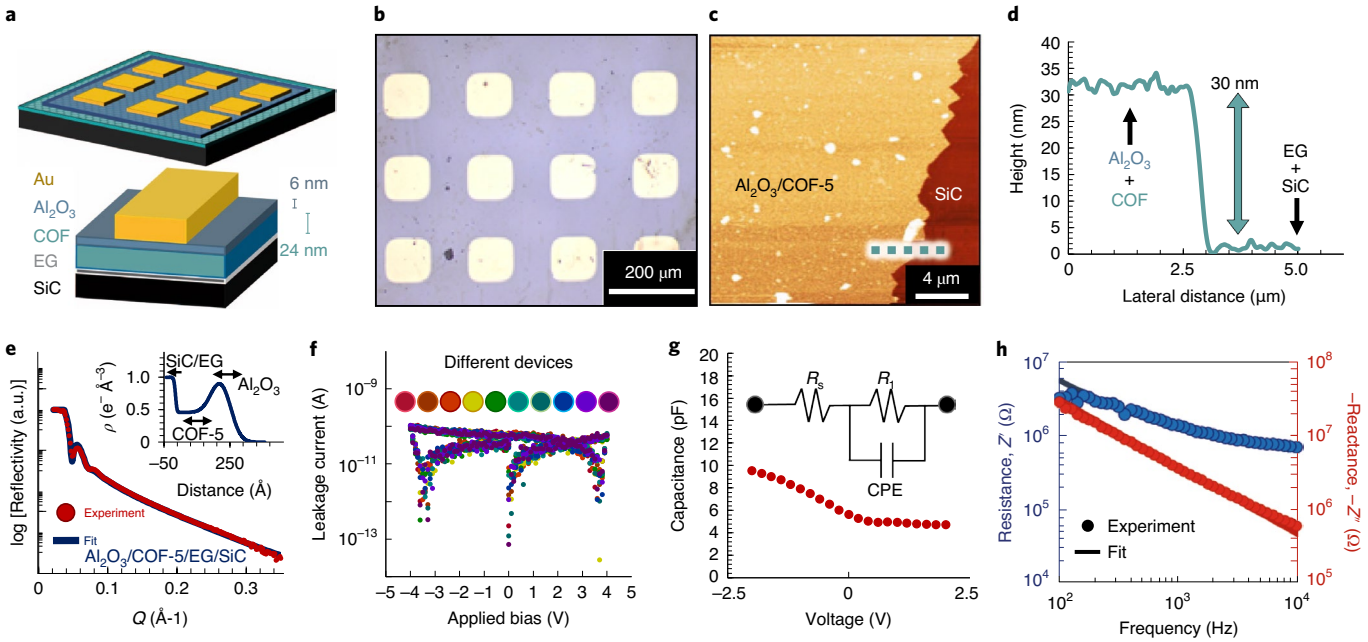

Fig. 3 | COF-5 dielectric layer impedance measurements. a, Schematic of Au-contacted Al_2O_3/COF-5 dielectric bilayer capacitors grown on EG/SiC wafers. **b**, Optical microscopy image of a patterned array of Au pads on full-coverage Al_2O_3/COF-5/EG/SiC. **c**, AFM micrograph of the Al_2O_3/COF-5 bilayer revealing a step edge at a scratch. **d**, Height profile extracted from the AFM teal line cut in **c**. **e**, X-ray reflectivity data and the model fit of the Al_2O_3/COF-5/EG/SiC layered structure. Inset: extracted electron density profile from the X-ray reflectivity fit. **f**, Leakage current versus the applied bias voltage across ten different COF devices. **g**, Capacitance of the Al_2O_3/COF-5 bilayer as a function of applied voltage measured at 1 kHz with a 100 mV signal. Inset: modelled equivalent circuit of impedance behaviour fit in **h**. CPE, constant phase element. **h**, Bode plots of the real (resistance, Z') and imaginary (reactance, Z'') impedance components and respective model fits.

(Fig. 3a,b). The thickness of the COF-5/Al_2O_3 bilayer (30 nm) was measured with AFM and cross-sectional scanning electron microscopy (Fig. 3c,d and Supplementary Fig. 44), which revealed that the COF-5 layer was 24 nm thick. The integrity of the COF-5/Al_2O_3 bilayer was confirmed by X-ray reflectivity measurements (Fig. 3e) that showed well-resolved electron density profiles of the SiC, Al_2O_3 and COF-5 layers, which suggests that these layers do not substantially intermix (Fig. 3e, inset). This observation is consistent with a homogeneous COF-5 film over the entire wafer with minimal intercalation of Al_2O_3.

COF-5 capacitors show a leakage current of less than 0.1 nA for an applied bias range of −4 V to +4 V (area of 10^4 μm^2) (Fig. 3f), which indicates robust dielectric layers. Effective capacitance was then extracted as ~6 pF at 0 V, with bias-dependent capacitance attributed to the quantum capacitance of graphene (Fig. 3g)[27]. Next, we examined the frequency dependence of the real (resistance, Z') and the imaginary (reactance, Z'') impedance (Fig. 3h), and fit this behaviour as a simplified resistor–capacitor circuit (Fig. 3g, inset), with R_1 (10 GΩ) determined from leakage measurements and fitting R_s to account for series resistance (64 kΩ) from the SiC substrate and contacts. Finally, the non-ideal nature of the COF-5/Al_2O_3 bilayer is represented as the constant phase element with a magnitude of 7.52 ± 0.12 pF and an ideality factor of 0.9. With the known thickness (6 nm) and dielectric constant of Al_2O_3 (k = 6.5) and the total capacitance of the COF-5/Al_2O_3 bilayer (5.64 pF), the capacitance and dielectric constant of the COF-5 layers are extracted as 5.99 pF and 1.62, respectively[27]. The excellent model fits and the nearly f^{-1} behaviour of reactance confirm the validity of the resistor–capacitor model (Fig. 3h). The capacitance was found to be uniform (within 10%) across the entire COF-5 film (Supplementary Fig. 49), which suggests excellent uniformity of the thin film. This measured k is consistent with the DFT-calculated COF-5 dielectric tensors. We also observe that this ultra-low-k dielectric constant is invariant with respect to atmosphere composition and temperature (−40 °C to +110 °C, Supplementary Figs. 50 and 51). Overall, these results show that thin, well-fabricated COF films function as low-k dielectric layers.

Thermal properties

COF thin films are found to be substantially more thermally conductive than previously studied low-k dielectrics. To measure the thermal properties of COF thin films with time-domain thermoreflectance, we first deposited Al transducer layers (see Supporting Information for a more detailed description of the measurement) onto several COF films of sub-100 nm thickness (Supplementary Fig. 57). From TDTR measurements, we extract the longitudinal sound speeds, heat capacities and cross-plane thermal conductivities of the COFs (Fig. 4a,b). Fitted TDTR data revealed that COF-5 and TP-COF have volumetric heat capacities of $C_{v,\,\mathrm{COF\text{-}5}} = 0.52 \pm 0.08\ \mathrm{J\,cm^{-3}\,K^{-1}}$ and $C_{v,\,\mathrm{TP\text{-}COF}} = 0.56 \pm 0.09\ \mathrm{J\,cm^{-3}\,K^{-1}}$ and cross-plane thermal conductivities of $\kappa_{\mathrm{COF\text{-}5}} = 1.03 \pm 0.15\ \mathrm{W\,m^{-1}\,K^{-1}}$ and $\kappa_{\mathrm{TP\text{-}COF}} = 0.89 \pm 0.14\ \mathrm{W\,m^{-1}\,K^{-1}}$ within a 95% confidence interval, respectively (Fig. 4b). These values are corroborated with FDTR measurements performed independently (Supplementary Figs. 50–53). We also find that the interfacial thermal conductances across the interfaces of COF/Al and COF/SLG (where SLG is single layer graphene) are quite high ($h_K > 100\ \mathrm{MW\,m^{-2}\,K^{-1}}$) (Supplementary Figs. 55–57), which highlights another advantage of COF films that are well interfaced to their underlying substrate.

Compared to other organic or porous materials, 2D COFs have unusually high thermal conductivities (Fig. 4d). This finding is consistent with the structural regularity, large porosities, strong interlayer interactions and low heat capacities of 2D COFs. From picosecond acoustics, we determine sound speeds for COF-5 (Fig. 4a,

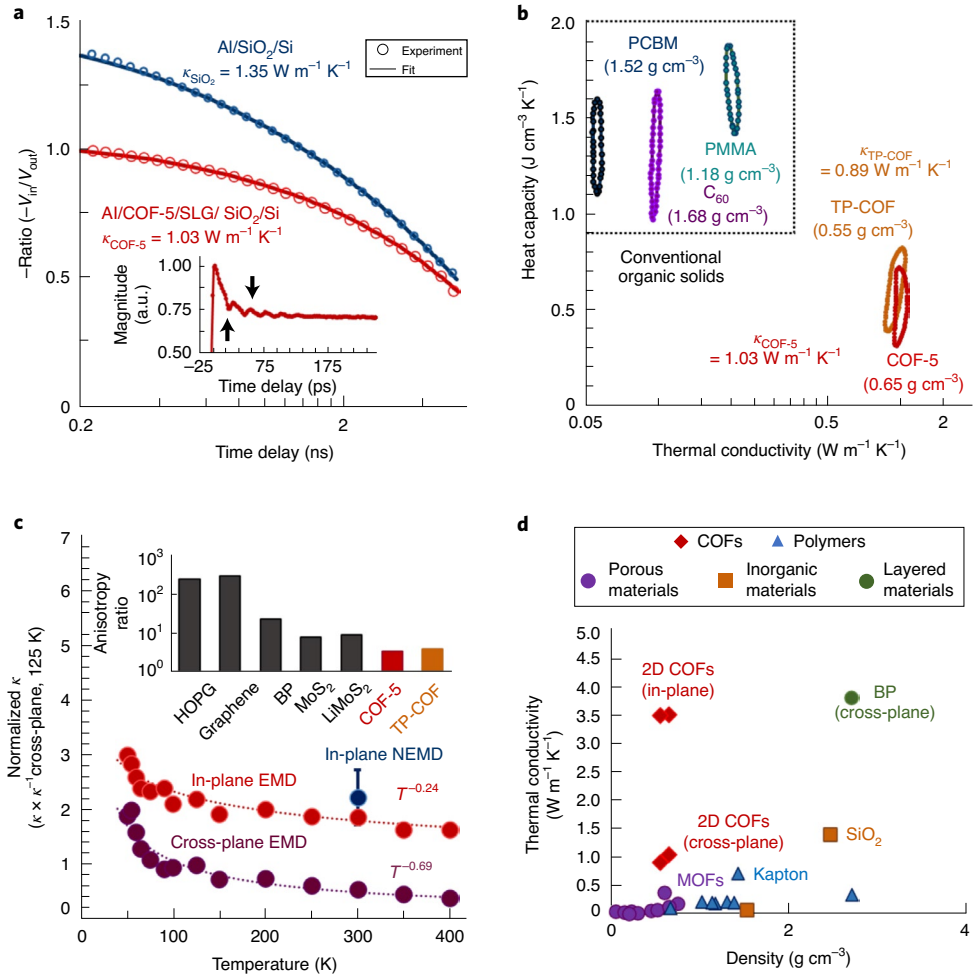

Fig. 4 | Thermal properties of 2D COF thin films. a, Characteristic TDTR data as a function of pump–probe delay time and analytical model fits. Inset: picosecond acoustics. **b**, Contour plots of thermal conductivity and heat capacity at a 95% confidence interval. **c**, Molecular dynamics simulations of temperature-dependent thermal conductivities. Dashed lines represent analytical fits generated from the temperature dependence shown. The error bar represents the variance in three independent simulations carried out for various computational domain lengths in the NEMD simulations. **d**, Density and thermal conductivity of common materials. Error bars for COF properties are found to be smaller than the size of the markers. BP, black phosphorus; EMD, equilibrium molecular dynamics; HOPG, highly oriented pyrolytic graphite; NEMD, non-equilibrium molecular dynamics; PCBM, phenyl-C_{61}-butyric acid methyl ester; PMMA, poly(methyl methacrylate).

inset) and TP-COF to be $2{,}000 \pm 300\,m\,s^{-1}$ and $1{,}900 \pm 300\,m\,s^{-1}$, respectively. These sound speeds are higher than those recently observed in metal–organic frameworks (MOFs) (for example, $1{,}184\,m\,s^{-1}$ for MOF-5) despite a porosity similar to those of the two COFs studied here[28,29]. These relatively high thermal conductivities and longitudinal sound speeds (compared to those of other porous materials) demonstrate how previously unobserved thermal properties arise from the covalently linked, layered, precisely porous structures of COFs.

Molecular dynamics simulations give additional insight into the high anisotropic thermal conductivities of COF-5. The cross-plane thermal conductivities predicted by molecular dynamics are slightly lower than the measured values (see Supporting Information for more discussion), which could be a consequence of the insufficiencies of the interatomic potential used to model our 2D COFs. However, these differences are equivalent in all crystallographic directions and so, through the same analysis, we extract an anisotropy ratio of 3.4 between in-plane and cross-plane COF-5 thermal conductivities (Fig. 4c). This anisotropy is valuable for thermally dissipative coatings, including in low-k dielectric layers, where device failure from thermal build-up can be mitigated (Supplementary Fig. 64). By this approach, we predict an in-plane thermal conductivity of $\kappa_{COF\text{-}5} = 3.5\,W\,m^{-1}\,K^{-1}$. These absolute thermal conductivities and anisotropy ratios are lower for 2D COFs than for other layered crystals (Fig. 4c, inset), which likely arises as a function of periodic voids in their van der Waals surface. The temperature-dependent thermal conductivities of COF-5 in the range of 50 K to 400 K are shown to exhibit a $T^{-0.24}$ and $T^{-0.69}$ dependence in the in-plane and cross-plane directions, respectively (Fig. 4c). These temperature dependencies suggest that anharmonic processes dictate the thermal transport in the cross-plane direction more heavily than in the in-plane direction[30].

Thermally conductive dielectrics

The 2D COFs overcome the traditional trade-off between dielectric permittivity and thermal conductivity that is found in all known low-k dielectric materials (Fig. 5). For example, dense amorphous metal oxides such as Al_2O_3 or HfO_2 are relatively thermally conductive compared to low-density aerogels, which are thermally insulating owing to their porous structure and tortuous

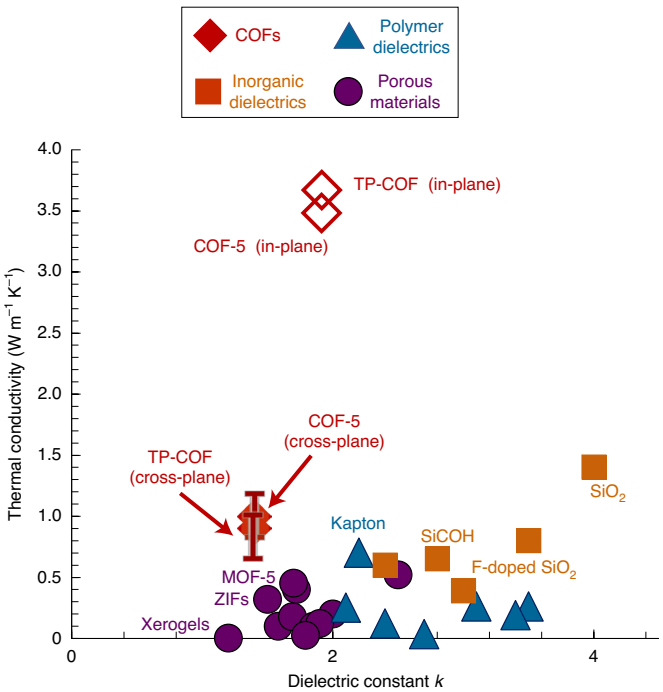

Fig. 5 | Meta-analysis of thermal conductivities in low-*k* dielectrics. Relation between thermal conductivity and dielectric constant for various materials. Filled diamonds are experimentally measured thermal conductivities and open diamonds are evaluated using computational techniques. For initial reports of the values included in the plot, see the Supplementary Information. Error bars for COF properties are found to be smaller than the size of the markers. ZIFs, zeolitic imidazolate frameworks.

solid networks[8,31,32]. Although the densities of 2D COFs are comparable to those of aerogels, their thermal conductivities are comparable to those of materials that are an order of magnitude denser, such as conventional amorphous metal oxide dielectrics[32]. This relatively high thermal conductivity is most likely driven by the well-interfaced van der Waals contact of porous 2D polymers that are arranged as eclipsed stacks. Based on additional molecular dynamics simulations performed on other boron-based 2D COFs (Supplementary Fig. 63), we find that the thermal conductivity of these systems is correlated to their van der Waals interactions and inversely related to their porosity. This suggests that smaller-pore COFs with large van der Waals surfaces will be highly thermally conductive. Furthermore, we suspect that the thermomechanical properties of 2D COFs could be modulated by the introduction of molecular guests, as has been observed in other porous materials, which unlocks the possibility of responsive materials[33,34]. The combined thermal resistances of these COF films (including both thermal conductivity and thermal boundary conductances) highlight 2D COFs as low-thermal-resistance, ultra-low-*k* thin films relative to traditionally studied low-*k* dielectrics.

Conclusions and outlook

In conclusion, we find that the combination of structural, thermal and electronic properties of 2D COFs make them promising as low-*k* dielectric layers. Specifically, we find that 2D COFs exhibit unusually high thermal conductivities for low-density, low-*k* dielectrics, a combination of properties that was recently identified by the *International Roadmap for Semiconductors*[4] as a prerequisite for next-generation integrated circuits. More broadly, these results demonstrate that exotic combinations of properties can be unlocked by using synthetic chemistry to generate structurally precise organic materials. Going forward, we expect that a broad investigation of 2D polymer properties is likely to yield technologically relevant materials across many application contexts.

Online content

Any methods, additional references, Nature Research reporting summaries, source data, extended data, supplementary information, acknowledgements, peer review information; details of author contributions and competing interests; and statements of data and code availability are available at https://doi.org/10.1038/s41563-021-00934-3.

Received: 15 June 2020; Accepted: 18 January 2021;
Published online: 18 March 2021

References

1. Krishtab, M. et al. Vapor-deposited zeolitic imidazolate frameworks as gap-filling ultra-low-*k* dielectrics. *Nat. Commun.* **10**, 3729 (2019).
2. Volksen, W., Miller, R. D. & Dubois, G. Low dielectric constant materials. *Chem. Rev.* **110**, 56–110 (2010).
3. Maex, K. et al. Low dielectric constant materials for microelectronics. *J. Appl. Phys.* **93**, 8793–8841 (2003).
4. *International Roadmap for Devices and Systems (IRDS)* (IEEE, 2017); https://irds.ieee.org/
5. Arden, W. M. The international technology roadmap for semiconductors—perspectives and challenges for the next 15 years. *Curr. Opin. Solid State Mater. Sci.* **6**, 371–377 (2002).
6. Miller, R. D. In search of low-*k* dielectrics. *Science* **286**, 421–423 (1999).
7. Veres, J., Ogier, S. D., Leeming, S. W., Cupertino, D. C. & Mohialdin Khaffaf, S. Low-*k* insulators as the choice of dielectrics in organic field-effect transistors. *Adv. Func. Mater.* **13**, 199–204 (2003).
8. Hopkins, P. E., Kaehr, B., Piekos, E. S., Dunphy, D. & Brinker, C. J. Minimum thermal conductivity considerations in aerogel thin films. *J. Appl. Phys.* **111**, 113532 (2012).
9. Erickson, K. J. et al. Thin film thermoelectric metal–organic framework with high Seebeck coefficient and low thermal conductivity. *Adv. Mater.* **27**, 3453–3459 (2015).
10. Xie, X. et al. Thermal conductivity, heat capacity, and elastic constants of water-soluble polymers and polymer blends. *Macromolecules* **49**, 972–978 (2016).
11. Kim, G.-H. et al. High thermal conductivity in amorphous polymer blends by engineered interchain interactions. *Nat. Mater.* **14**, 295–300 (2015).
12. Evans, A. M. et al. Buckling of two-dimensional covalent organic frameworks under thermal stress. *Ind. Eng. Chem. Res.* **58**, 9883–9887 (2019).
13. Bisbey, R. P. & Dichtel, W. R. Covalent organic frameworks as a platform for multidimensional polymerization. *ACS Cent. Sci.* **3**, 533–543 (2017).
14. Sick, T. et al. Oriented films of conjugated 2D covalent organic frameworks as photocathodes for water splitting. *J. Am. Chem. Soc.* **140**, 2085–2092 (2018).
15. Colson, J. W. et al. Oriented 2D covalent organic framework thin films on single-layer graphene. *Science* **332**, 228–231 (2011).
16. Burke, D. W. et al. Acid exfoliation of imine-linked covalent organic frameworks enables solution processing into crystalline thin films. *Angew. Chem. Int. Ed.* **59**, 5165–5171 (2019).
17. Chen, X. et al. High-lithium-affinity chemically exfoliated 2D covalent organic frameworks. *Adv. Mater.* **31**, 1901640 (2019).
18. Dey, K. et al. Selective molecular separation by interfacially crystallized covalent organic framework thin films. *J. Am. Chem. Soc.* **139**, 13083–13091 (2017).
19. Sasmal, H. S. et al. Covalent self-assembly in two dimensions: connecting covalent organic framework nanospheres into crystalline and porous thin films. *J. Am. Chem. Soc.* **141**, 20371–20379 (2019).
20. Rodríguez-San-Miguel, D. & Zamora, F. Processing of covalent organic frameworks: an ingredient for a material to succeed. *Chem. Soc. Rev.* **48**, 4375–4386 (2019).
21. Shao, P. et al. Flexible films of covalent organic frameworks with ultralow dielectric constants under high humidity. *Angew. Chem. Int. Ed.* **57**, 16501–16505 (2018).
22. Evans, A. M. et al. Seeded growth of single-crystal two-dimensional covalent organic frameworks. *Science* **361**, 52–57 (2018).
23. Li, H. et al. Nucleation–elongation dynamics of two-dimensional covalent organic frameworks. *J. Am. Chem. Soc.* **142**, 1367–1374 (2020).
24. Smith, B. J. et al. Colloidal covalent organic frameworks. *ACS Cent. Sci.* **3**, 58–65 (2017).
25. Cao, S., Li, B., Zhu, R. & Pang, H. Design and synthesis of covalent organic frameworks towards energy and environment fields. *Chem. Eng. J.* **355**, 602–623 (2019).

26. Ikeda, M., Takeuchi, M. & Shinkai, S. Unusual emission properties of a triphenylene-based organogel system. *Chem. Commun.* **9**, 1354–1355 (2003).
27. Sangwan, V. K. et al. Quantitatively enhanced reliability and uniformity of high-κ dielectrics on graphene enabled by self-assembled seeding layers. *Nano Lett.* **13**, 1162–1167 (2013).
28. Huang, B. L., McGaughey, A. J. H. & Kaviany, M. Thermal conductivity of metal-organic framework 5 (MOF-5): Part I. Molecular dynamics simulations. *Int. J. Heat Mass Transf.* **50**, 393–404 (2007).
29. Wang, X., Liman, C. D., Treat, N. D., Chabinyc, M. L. & Cahill, D. G. Ultralow thermal conductivity of fullerene derivatives. *Phys. Rev. B* **88**, 075310 (2013).
30. Klemens, P. G. The scattering of low-frequency lattice waves by static imperfections. *Proc. Phys. Soc. A* **68**, 1113 (1955).
31. Gaskins, J. T. et al. Investigation and review of the thermal, mechanical, electrical, optical, and structural properties of atomic layer deposited high-*k* dielectrics: beryllium oxide, aluminum oxide, hafnium oxide, and aluminum nitride. *ECS J. Solid State Sci. Technol.* **6**, N189 (2017).
32. Scott, E. A., Gaskins, J. T., King, S. W. & Hopkins, P. E. Thermal conductivity and thermal boundary resistance of atomic layer deposited high-*k* dielectric aluminum oxide, hafnium oxide, and titanium oxide thin films on silicon. *APL Mater.* **6**, 058302 (2018).
33. Giri, A., Tomko, J., Gaskins, J. T. & Hopkins, P. E. Large tunability in the mechanical and thermal properties of carbon nanotube-fullerene hierarchical monoliths. *Nanoscale* **10**, 22166–22172 (2018).
34. McGaughey, A. J. H. & Kaviany, M. Thermal conductivity decomposition and analysis using molecular dynamics simulations: Part II. Complex silica structures. *Int. J. Heat Mass Transf.* **47**, 1799–1816 (2004).

Methods

General synthesis of COF films. First, a graphene-coated Si/SiO_2 substrate (1 cm^2, UniversityWafer) was placed into a scintillation vial. Then, solutions of HHTP (2 mM) and bisboronic acid (3 mM) were prepared separately in a solvent blend of 80:16:4 (vol) CH_3CN:1,4-dioxane:1,3,5-trimethylbenzene. These solutions were then filtered to remove any insoluble particulates. These solutions were then added in a 1:1 volume ratio to the substate-containing scintillation vial, producing a 20 ml solution of 1 mM HHTP and 1.5 mM bisboronic acid. This scintillation vial was then sealed and heated to 80 °C for 24 h, after which a milky suspension had formed in the scintillation vial. Approximately 90% of the solution was then decanted and diluted with fresh 80:16:4 (vol) CH_3CN:1,4-dioxane:1,3,5-trimethylbenzene. This procedure was repeated three times to sufficiently dilute any colloidal species present in solution. The wafer was then removed from solvent with forceps and allowed to dry in air, which produced a conformal coating on the graphene substrate.

Grazing-incidence X-ray scattering. All GI-WAXS described here was performed at the Advanced Photon Source at Argonne National Laboratory using Beamline 8-ID-E under vacuum. The crystallites were irradiated until the maximum pixel was 80% saturated at an incidence angle of 0.14° and using 10.92 keV ($\lambda = 1.135$ Å) X-rays. The scattering was recorded on a Pilatus 1M detector located 228 mm from the sample. In some cases, silicon substrate scatter was observed. The raw images were merged, pixel coordinates were transformed to q-space, and line cuts were generated using GIXSGUI version 1.7.3 for MATLAB[35].

Density functional theory. The macroscopic static dielectric tensors considering the electronic contribution[36] are calculated with the DFT method at the PBE level using the Vienna Ab initio Simulation Package (VASP) version 5.4.1 (ref. [37]) with D3 vdW corrections. Γ-centred Monkhorst–Pack k-meshes are adopted in both geometry optimizations and self-consistent field calculations (Supplementary Table 1). The convergence criterion for the total energy is 10^{-8} eV and 0.01 eV $Å^{-1}$ for the forces. Gaussian smearing is 0.01 eV. The lattice parameters after geometry optimization of each COF are shown in Supplementary Table 2. The off-diagonal components in the calculated macroscopic static dielectric tensors are negligibly small.

Fluorescence spectroscopy. Emission and excitation spectra were recorded on a Horiba Jobin Yvon Fluorolog-3 fluorescence spectrophotometer equipped with a 450 W Xe lamp, emission and excitation polarizer, double excitation and double emission monochromators, and a digital photon-counting photomultiplier. Correction for variations in lamp intensity over time and with wavelength was achieved by using a solid-state silicon photodiode as the reference. The spectra were further corrected for variations in photomultiplier response with wavelength and for the path difference between the sample and the reference by multiplication with emission correction curves generated on the instrument. To collect polarization-dependent emission spectra of the 2D COF films, films were mounted in a proprietary film holder and a polarizer was placed in the emission path. When emission polarization was noted as 'normalized', we divided the intensity of all emission intensities by the maximum emission intensity.

Device measurement. Impedance measurements were carried out by a Solartron 1260 impedance analyser using an a.c. amplitude of 100 mV in a frequency range of 100 Hz to 10 kHz. This frequency range was chosen because the signal was too noisy below 100 Hz and series resistance from the SiC wafer interfered with measurements above 10 kHz. Au pads were contacted by tungsten cat-whisker soft probes (SE-SM, Signatone) to avoid puncturing the COF dielectric. Capacitance–frequency (C–f) measurements were performed at zero d.c. bias, and capacitance–voltage (C–V) measurements were conducted at 1 kHz. Capacitance values were verified independently by using the C–V module of a Keithley Instruments 4200 Semiconductor Characterization System (SCS). Leakage measurements were also carried out by using the 4200 SCS with a remote current preamplifier.

Heat capacity and thermal conductivity measurements. In our TDTR set-up, sub-picosecond laser pulses emanate from a Ti:sapphire oscillator at a repetition rate of 80 MHz. The pulses are separated into a pump path that heats up the sample and a time-delayed probe path that is reflected from the Al transducer. The reflected probe beam provides a measure of the change in the thermoreflectance caused by the decay of the thermal energy deposited by the pump beam. A modulation of 8.8 MHz is applied by an electro-optic modulator on the pump beam, and the ratio of the in-phase to out-of-phase signals of the reflected probe beam is recorded at that frequency by a lock-in amplifier ($-V_{in}/V_{out}$) for up to 5.5 ns after the initial heating event. The pump and probe beams are focused on the Al transducer at $1/e^2$ radii values of 10 μm and 5 μm, respectively. To simultaneously measure the thermal conductivity and heat capacity of our COFs, we fit a three-layer thermal model to our experimental data. We also perform FDTR measurements on our COF-5 sample. Similar to TDTR, FDTR is a laser-based metrology implemented to measure thermal properties of a sample. The Au-coated sample is periodically heated via a sinusoidally modulated (100 kHz to 5 MHz) pump laser at 488 nm wavelength. The temperature of the sample will fluctuate with the same frequency as the pump laser, but with a time delay. This phase delay is characteristic of the thermal properties of the sample. The temperature is measured using a concentric probe laser (532 nm), which is sensitive to the thermoreflectance of Au. The frequency-dependent time delay that is measured as a phase delay of the reflected probe laser with respect to the pump laser modulation frequency is measured with a photodiode connected to a lock-in amplifier (Supporting Information).

Molecular dynamics simulation. Our molecular dynamics simulations are performed with the LAMMPS code (LAMMPS/7Aug2019)[38], and the interatomic interactions are described by the adaptive intermolecular reactive empirical bond order (AIREBO) potential[39]. We apply periodic boundary conditions in all directions. The computational domains are equilibrated under the Nosé–Hoover thermostat and barostat[40] (which is the NPT integration with the number of particles, pressure and temperature of the system held constant) for a total of 1 ns at 0 bar pressure. Following the NPT integration, an NVT integration (with constant number of particles, volume and temperature) is prescribed to fully equilibrate the structures at the desired temperature for another 1 ns. Note that we prescribe a time step of 0.5 fs for all our simulations. After equilibration, the thermal conductivities of our COFs at different temperatures are predicted via the Green–Kubo approach under the equilibrium molecular dynamics framework. In this formalism, the thermal conductivities of our COFs along the x and y (in-plane) and z (cross-plane) directions are calculated as

$$\kappa_{x,y,z} = \frac{1}{k_{BVT}^2}\int_0^\infty < S_{x,y,z}(t) \cdot S_{x,y,z}(0) > \mathrm{d}t \qquad (1)$$

where t is time, T and V are the temperature and volume of the systems, respectively, and $<S_{x,yz}(t)S_{x,yz}(0)>$ is the component of the heat current autocorrelation function (HCACF) in the prescribed directions.

Data availability

Source data are provided with this paper. Additional data are available from the corresponding authors upon request.

References

35. Jiang, Z. GIXSGUI: a MATLAB toolbox for grazing-incidence X-ray scattering data visualization and reduction, and indexing of buried three-dimensional periodic nanostructured films. *J. Appl. Crystallogr.* **48**, 917–926 (2015).
36. Gajdoš, M., Hummer, K., Kresse, G., Furthmüller, J. & Bechstedt, F. Linear optical properties in the projector-augmented wave methodology. *Phys. Rev. B* **73**, 045112 (2006).
37. Perdew, J. P., Burke, K. & Ernzerhof, M. Generalized gradient approximation made simple. *Phys. Rev. Lett.* **77**, 3865–3868 (1996).
38. Plimpton, S. Fast parallel algorithms for short-range molecular dynamics. *J. Comput. Phys.* **117**, 1–19 (1995).
39. Stuart, S. J., Tutein, A. B. & Harrison, J. A. A reactive potential for hydrocarbons with intermolecular interactions. *J. Chem. Phys.* **112**, 6472–6486 (2000).
40. Hoover, W. G. & Posch, H. A. Direct measurement of Lyapunov exponents. *Phys. Lett. A* **113**, 82–84 (1985).

Acknowledgements

W.R.D., J.-L.B. and F.W. thank the Army Research Office of the United States for a Multidisciplinary University Research Initiatives (MURI) award under grant no. W911NF-15-1-0447. A.M.E. is supported by a National Science Foundation (NSF) Graduate Research Fellowship under grant no. DGE-1324585. N.P.B. also acknowledges an NSF Graduate Research Fellowship. A.G. and P.E.H. appreciate support from the Office of Naval Research (grant no. N00014-20-1-2686). M.B., J.A.M. and A.J.H.M. gratefully acknowledge support from the Army Research Office, grant W911NF-17-1-0397. The electron microscopy work was supported by the United States Department of Energy (DOE DE-SC0019356), and the impedance spectroscopy work was supported by the NSF (DMR-1720139). This study made use of the Integrated Molecular Structure Education and Research Center (IMSERC) and the Electron Probe Instrumentation Center (EPIC) at Northwestern University, both of which have received support from the Soft and Hybrid Nanotechnology Experimental (SHyNE) Resource (NSF NNCI-1542205 and NSF ECCS1542205, respectively), the Materials Research Science and Engineering Center (NSF DMR-1720139), the State of Illinois, and the International Institute for Nanotechnology. Portions of this work were performed at the DuPont–Northwestern–Dow Collaborative Access Team (DND-CAT) located at Sector 5 and Sector 8 of the Advanced Photon Source (APS). DND-CAT is supported by Northwestern University, E.I. DuPont de Nemours & Co. and the Dow Chemical Company. This research used resources of the Advanced Photon Source and Center for Nanoscale Materials, both of which are DOE Office of Science User Facilities operated for the DOE Office of Science by Argonne National Laboratory under contract no. DE-AC02-06CH11357. Resources at the Advanced Photon Source were funded by the

NSF under award no. 0960140. This research used resources of the Advanced Light Source, a DOE Office of Science User Facility under contract no. DE-AC02-05CH11231.

Author contributions

A.M.E. prepared and characterized all COF films. A.G. performed all thermal property characterization and simulations. V.K.S. prepared COF-5 devices and performed impedance spectroscopy. S.X. and H.L. performed and interpreted density functional theory calculations. M.B. performed thermal property characterization. C.G.T.-C. performed and interpreted the X-ray reflectivity experiments. H.B.B. performed synchrotron X-ray scattering experiments. M.S.R. prepared EG/SiC substrates used for COF devices. N.P.B. imaged the COF devices using scanning electron microscopy. E.V. assisted with monomer syntheses. D.W.B. assisted with synchrotron X-ray characterization. V.K.S., H.L., M.J.B., F.W., J.-L.B., J.A.M., A.J.H.M., M.C.H., W.R.D. and P.E.H. supervised this work. All authors contributed to the conception of the study, data interpretation and manuscript preparation.

Competing interests

Northwestern University and the University of Virginia have filed a preliminary patent application (provisional application no. 6314014) related to the discoveries disclosed here.

Additional information

Supplementary information The online version contains supplementary material available at https://doi.org/10.1038/s41563-021-00934-3.

Correspondence and requests for materials should be addressed to W.R.D. or P.E.H.

Peer review information *Nature Materials* thanks the anonymous reviewers for their contribution to the peer review of this work.

Reprints and permissions information is available at www.nature.com/reprints.